



Article

Integrated DC/DC Converter Topology Study for Fuel Cell Hybrid Vehicles with Two Energy Sources

Weijin Xie ^{1,2}, Wenguang Luo ^{1,2,*}  and Yongxin Qin ^{1,*}

¹ School of Automation, Guangxi University of Science and Technology, Liuzhou 545000, China

² Guangxi Key Laboratory of Auto Parts and Vehicle Technology, Guangxi University of Science and Technology, Liuzhou 545000, China

* Correspondence: wgluo@gxust.edu.cn (W.L.); 100000320@gxust.edu.cn (Y.Q.); Tel.: +86-772-268-4191 (W.L.)

Abstract: Conventional hybrid vehicles with two energy sources require two separate on-board DC/DC converters to connect the battery and the fuel cell, which have the disadvantages of large size, high cost, high losses and few applicable operating conditions. To address this situation, this paper proposes an optimized on-board integrated DC/DC converter with a non-isolated multi-port scheme that integrates a unidirectional port for the fuel cell and a bidirectional port for the battery and load. This can achieve a combined energy supply and recovery with a single integrated converter, effectively overcoming the above disadvantages. The optimized converter topology is relatively simple, and the magnetic losses of the transformer are removed. Furthermore, the switched capacitor is introduced as a voltage doubling unit to achieve high-gain output, so the fuel cell and battery voltage demand levels are reduced under the same load conditions. In addition, it has superior performance in system energy management for hybrid vehicles, which can distribute power and switch operating states by controlling the on/off of switching devices to make it suitable for five driving conditions. This paper discusses in detail the operating principles of the converter and analyzes its steady-state performance under five operating modes, derives its dynamic model, and proposes a proportional-integral control scheme. Finally, the simulation model of the topology is built by Matlab/Simulink software to verify the converter operation in each driving state, and the simulation experimental results verify the applicability of the proposed integrated DC/DC converter topology.

Keywords: hybrid vehicle; integrated converter; voltage doubling unit; high gain; multiple operating states



Citation: Xie, W.; Luo, W.; Qin, Y. Integrated DC/DC Converter Topology Study for Fuel Cell Hybrid Vehicles with Two Energy Sources. *World Electr. Veh. J.* **2023**, *14*, 9. <https://doi.org/10.3390/wevj14010009>

Academic Editors: Jianfei Chen, Liyan Zhu, Chen Duan and Haibo Huang

Received: 14 November 2022
Revised: 22 December 2022
Accepted: 26 December 2022
Published: 29 December 2022



Copyright: © 2022 by the authors. Licensee MDPI, Basel, Switzerland. This article is an open access article distributed under the terms and conditions of the Creative Commons Attribution (CC BY) license (<https://creativecommons.org/licenses/by/4.0/>).

1. Introduction

With the increasingly severe problems of environmental pollution and energy shortage, the development of electric vehicles has received widespread attention, but the imperfect development of its charging technology has given rise to concerns about its cruising mileage. Thanks to the advantages of fast gas filling, no pollution, and the high energy conversion rate of fuel cells [1,2], hybrid cars with two energy sources, fuel cell and battery, not only eases concerns about mileage anxiety, but also the disadvantage of the slow power response of fuel cells can be compensated by the another energy source, the battery [3]. Therefore, fuel cell hybrid vehicles with two energy sources have become one of the hot spots in the development of new-energy vehicles nowadays.

In the conventional multi-energy structure of fuel cell hybrid cars, the power transmission circuit is composed of a plurality of dual-port DC/DC converters. However, the more DC/DC converters, there will be higher system power loss, which is not conducive to the integration and miniaturization of on-board devices. So, the key point of research for hybrid vehicle converters is to simplify the structure of the circuit. Multi-port integrated DC/DC converter has the advantages of flexible energy distribution, simple structure, and low cost [4], and depending on whether there is an electrical isolation circuit formed

by a transformer between the ports or not, it is divided into three kinds of structures: isolated topology, semi-isolated topology, and non-isolated topology. Isolated topology can easily achieve multi-port transformation, and its ports can be easily expanded and modularized [5,6], having strong anti-interference ability. Nevertheless, the large size of the transformer also leads to high power cycle losses and design costs, especially for high-frequency and high-power transmission conditions [7,8]. Semi-isolated topology makes it easy to implement circuit integration using multiplexing power devices [9,10], but it still suffers from the drawback that magnetic losses cannot be reduced. And non-isolated topology lacking electromagnetic winding, is the simplest circuit structure, has lower power losses and more concentrated power density, and is an easier way to implement circuit integration.

However, the disadvantages cannot be ignored, such as the topology's ports being difficult to expand, its small single-stage conversion gain, the few applicable operating states, that each power cannot be supplied separately, that energy distribution is not possible, that leakage energy of coupled devices requires additional circuitry for elimination, the excessive ripple and inrush current, etc.

Considering these problems, the research on improving the on-board multi-port integrated converter has become a hot topic nowadays. In the literature [11], the use of pulse power supply units for direct port construction is mentioned, as well as the single-level power conversion between ports. In [12], a means of adding a few power devices into the Cuk topology to extend the energy storage ports is introduced. In [13–15], researchers connected the auxiliary power supply circuit in series with the main energy source to achieve a higher voltage gain, while fewer devices also made it more efficient. A kind of four-port converter in [16] improves the applicability of the topology by adding a low-voltage output port. The literature [17] gives an idea of using complementary pulse conduction to reduce conduction losses. A method based on synchronous rectification control to achieve power sizing of the port is presented in [18]. In [19–22], they simplify the topology by multiplexing the inductors, and the coupling inductor and switching capacitor improve the voltage gain while also giving itself low current ripple and soft switching characteristics. Switched capacitors are also introduced as voltage-doubling elements in order to increase the voltage gain too in [23–26]. The literatures [27,28] introduce bootstrap circuits capable of multi-state operation. In one study [29], a phase-shifted carrier modulation method is proposed to suppress the current ripple and reduce the size of the topology device by a significant amount. On the other hand, another study [30] describe in detail the performance analysis methods for various operating states of the non-isolated converters in continuous conduction conditions, perform stability analysis, and give a scheme for dynamic model calculations.

By pulling together the ideas mentioned above, for fuel cell hybrid vehicles, this paper proposes the solution of an improved non-isolated three-port integrated converter, which can be well-used effectively in the dual-energy source structure of the fuel cell and battery. Compared to traditional multi-energy structure converters, this proposed topology has a simpler and more compact structure, shorter power conversion paths and higher integration. In this solution, the voltage doubling unit is adopted to achieve higher output gain which can effectively reduce the input energy source voltage level, and the auxiliary circuits to suppress capacitive inrush currents is also be used, which can enhance safety. Moreover, this solution can apply to other working conditions, and, at the same time, can make more reasonable power distributions and can increase the system output power.

2. Improved Converter Topological Structure and Operating Principle

2.1. Topological Structure

The proposed structure of the integrated converter for hybrid vehicles is shown in Figure 1. The input ports of the converter topology are fuel cell (main energy) and battery (auxiliary energy) ports, and the output port is the bus connected to the inverter. Fuel cell

voltage, battery voltage, and output voltage are respectively marked by V_{fc} , V_{bat} , and u_o , and the relationship between these values is as follows: $V_{fc} < V_{bat} < u_o$.

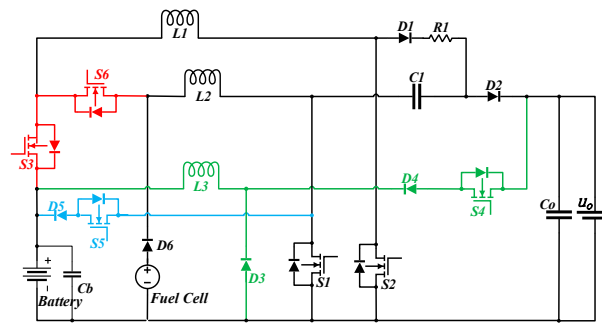


Figure 1. The Structure of Integrated Converter for Fuel Cell Hybrid Vehicle.

In the structure shown in Figure 1, the forward high-gain circuit consists of two booster inductors, L_1 and L_2 , and switched capacitor C_1 , and a negative temperature coefficient (NTC) thermistor R_1 is used to inhibit the current surge in the capacitor at the moment of turn-on. In addition, the inductor L_2 , which, with the switch S_5 , is used again to form a charging loop from the main energy to auxiliary energy. Switch S_4 controls the feedback circuit from the output port to the auxiliary energy. Switches S_3 and S_6 control the operation of the battery and the opening of the dual-source operating state.

2.2. Operating Principle

As shown in Figure 2, this converter topology works on continuous conduction conditions with five different working states. State 1 is the fuel-cell-energy operating state. State 2 is the battery energy operating state. State 3 is a hybrid dual-energy operating state. State 4 is the battery charging state. State 5 is the feedback state.

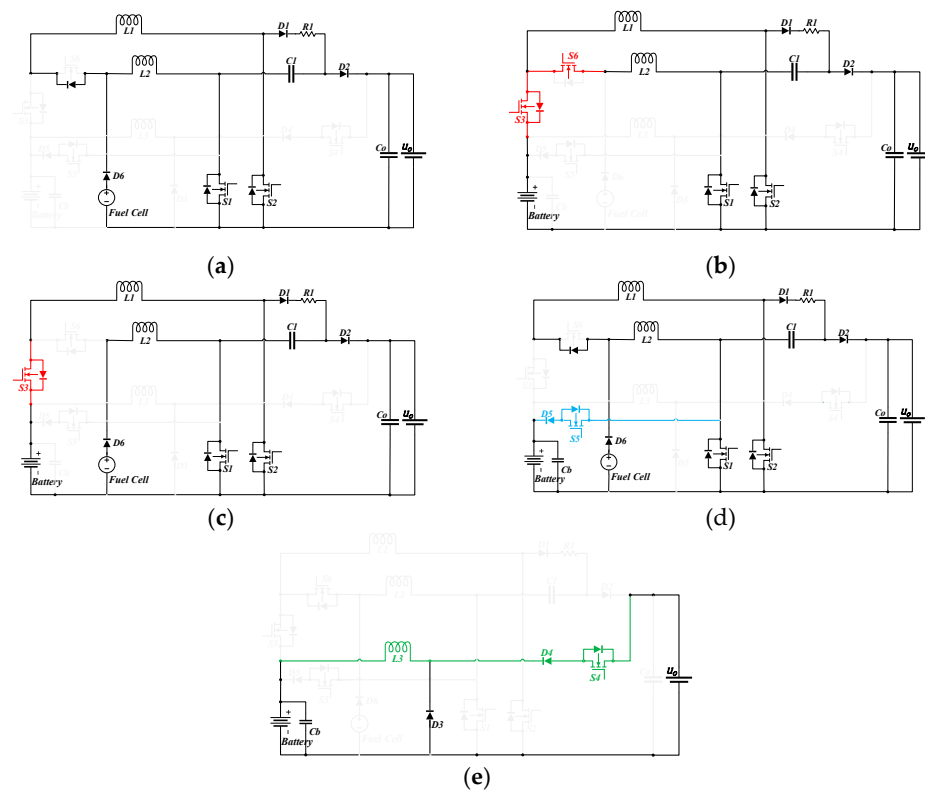


Figure 2. Equivalent circuits of five different operating states: (a) State 1; (b) State 2; (c) State 3; (d) State 4; (e) State 5.

1. State 1:

In this state, switch S3 and S6 and the anti-parallel diode of S3 are all turned off, while the anti-parallel diode of S6 is turned on. Its equivalent circuits are shown in Figure 2a which has three modes:

- Mode 1:

Switch S1 is turned on but S2 is turned off, the inductor L_2 is charged while inductor L_1 discharges to capacitor C_1 , and the load R_o supplied by capacitor C_o . It can be deduced that $u_{L1} = V_{fc} - u_{c1} - i_{r1}R_1$, $u_{L2} = V_{fc}i$

- Mode 2:

Switch S1 and S2 are both turned on, the inductors L_1 and L_2 are charged, the load R_o is still supplied by capacitor C_o . It can be deduced that $u_{L1} = u_{L2} = V_{fc}i$

- Mode 3:

Switch S2 is turned on and S1 is turned off, the inductor L_1 is charged, while the inductor L_2 and capacitor C_1 discharge to the load R_o together. It can be deduced that $u_{L1} = V_{fc}$, $u_{L2} = V_{fc} + u_{c1} - u_o$.

2. State 2:

In this state, switches S3 and S6 are always turned on, and the diode D6 is cut off by voltage clamping. The equivalent circuit is shown in Figure 2b, its working mode is exactly the same as in state 1, in which only the input source is different. As a result, we will not introduce this state again.

3. State 3:

In this state, switch S3 is always turned on, while the anti-parallel diode of S6 is cut off by voltage clamping. The equivalent circuit, which has four modes, is shown in Figure 2c which has four modes.

- Mode 1:

Switch S1 is turned on and S2 is turned off, the inductor L_2 is charged while inductor L_1 discharges to capacitor C_1 , and the load R_o supplied by capacitor C_o . It can be deduced that $u_{L1} = V_{bat} - u_{c1} - i_{r1}R_1$, $u_{L2} = V_{fc}i$

- Mode 2:

Switch S1 and S2 are turned on, the inductors L_1 and L_2 are charged, the load R_o is still supplied by capacitor C_o . It can be deduced that $u_{L1} = V_{bat}$, $u_{L2} = V_{fc}i$

- Mode 3:

Switch S2 is turned on and S1 is turned off, the inductor L_1 is charged, while the inductor L_2 and capacitor C_1 discharge to the load R_o together, it can be deduced that $u_{L1} = V_{bat}$, $u_{L2} = V_{fc} + u_{c1} - u_o$

- Mode 4:

Switch S1 and S2 are turned off, the fuel cell circuit will be connected in parallel with the battery circuit. It can be deduced that $u_{L1} = V_{bat} - u_o - i_{r1}R_1$, $u_{L2} = V_{fc} + u_{c1} - u_o$.

4. State 4:

In this state, switches S3 and S6 are turned off, while the anti-parallel diode of S3 is cut off by voltage clamping and the anti-parallel diode of S6 is turned on. The equivalent circuit is shown in Figure 2d, followed by its three operating modes.

- Mode 1:

Switch S2 and S5 are turned off and the switch S1 is turned on, so the inductor L_2 can be charged and L_1 discharges to capacitor C_1 while the load resistance R_o is supplied by capacitor C_o . It can be deduced that $u_{L1} = V_{fc} - u_{c1} - i_{r1}R_1$, $u_{L2} = V_{fc}i$

- Mode 2:

Switch S1 and S2 are turned off and the switch S5 is turned on, the load circuit is connected in parallel with the battery, so the inductor L_2 discharges to the load R_o , and capacitors C_1 is charged by the electric potential difference between the load and the battery, it can be deduced that $u_{L1} = V_{fc} - u_o$, $u_{L2} = V_{fc} - V_{bat}$, $u_{c1} = u_o - V_{bat}$;

- Mode 3:

Switch S2 and S5 are turned on but S1 is turned off, the inductor L_1 is charged, while L_2 discharges to the battery port and load in series with the capacitor C_1 simultaneously. It can be deduced that $u_{L1} = V_{fc}$, $u_{L2} = V_{fc} - V_{bat}$;

5. State 5:

Diodes D2 and D5 are cut off by voltage clamping in this state, as the equivalent circuit is shown in Figure 2e, which has the same two operating modes as the Buck converter.

- Mode 1:

Switch S4 is turned on. Meanwhile, the inductor L_3 and the battery port are charged by the feedback-load. It can be deduced that $u_{L3} = u_o - V_{bat}$;

- Mode 2:

Switch S4 is turned off, then the inductor L_3 is renewed by diode D3. It can be deduced that $u_{L3} = V_{bat}$.

In order to simplify the hybrid vehicle's energy distribution control strategy, this paper only discusses the problem of the equal duty cycles of S1 and S2 when the fuel cell or battery acts separately, and the different duty cycles of S1 and S2 when the fuel cell works with the battery for power distribution.

3. Steady-State Analysis

The corresponding voltages of the three ports of the integrated converter topology proposed in this paper are V_{fc} , V_{bat} , and u_o , and the output voltage in different states is determined by the duty cycle. NTC thermistor resistance value decreases as the temperature rises due to instantaneous high current conduction, so it is assumed that the thermistor resistance value and voltage ripple of capacitors C_1 and C_o can be neglected under steady-state conditions. If we consider the switching device as an ideal device, then, in a cycle, then there is an input-output relationship for each operating state as described below.

3.1. Topology-Gain Analysis

3.1.1. State 1

The input voltage in this state is V_{fc} , and the duty cycle of switch S1 and S2 is D . By applying the volt-second balance law over the inductors L_1 and L_2 , we have:

$$V_{fc}DT + (V_{fc} - u_{c1})(1 - D)T = 0 \quad (1)$$

$$V_{fc}DT + (V_{fc} + u_{c1} - u_o)(1 - D)T = 0 \quad (2)$$

the voltage across capacitor C_1 and the output voltage can be derived from Equations (1) and (2) as follows.

$$u_{c1} = \frac{1}{1 - D}V_{fc} \quad (3)$$

$$u_o = \frac{2}{1 - D}V_{fc} \quad (4)$$

3.1.2. State 2

The input voltage in this state is V_{bat} , and the duty cycle of switch S1 and S2 is D . By applying the volt-second balance law over the inductors L_1 and L_2 , we have:

$$V_{bat}DT + (V_{bat} - u_{c1})(1 - D)T = 0 \quad (5)$$

$$V_{bat}DT + (V_{bat} + u_{c1} - u_o)(1 - D)T = 0 \quad (6)$$

the voltage across capacitor C_1 and the output can be derived from Equations (5) and (6) as follows.

$$u_{c1} = \frac{1}{1 - D}V_{bat} \quad (7)$$

$$u_o = \frac{2}{1 - D}V_{bat} \quad (8)$$

3.1.3. State 3

In this state, V_{fc} and V_{bat} are the input voltages of converter circuit; meanwhile, d_1 and d_2 are the duty cycle of switches S1 and S2. The volt-second balance analysis of the inductor is divided into three cases: $d_1 + d_2 \geq 1$, $d_1 + d_2 < 1$ while $d_1 > d_2$, and $d_1 + d_2 < 1$ while $d_1 < d_2$.

When $d_1 + d_2 \geq 1$,

$$V_{bat}d_2T + (V_{bat} - u_{c1})(1 - d_2)T = 0 \quad (9)$$

$$V_{fc}d_1T + (V_{fc} + u_{c1} - u_o)(1 - d_1)T = 0 \quad (10)$$

the voltage across capacitor C_1 and the output voltage can be derived from Equations (11) and (12) as follows.

$$u_{c1} = \frac{1}{1 - d_2}V_{bat} \quad (11)$$

$$u_o = \frac{1}{1 - d_1}V_{fc} + \frac{1}{1 - d_2}V_{bat} \quad (12)$$

If $d_1 + d_2 < 1$ and $d_1 > d_2$, assume the time interval when the switch S1 is on and S2 is off, while the switching capacitor C_1 is charged by the battery, as a proportion of the cycle T is φ . The modulation method should make φ increase as much as possible to ensure that the power of the battery is saved into the capacitor C_1 , and, because d_1 is greater than d_2 , so $d_1 - d_2 \leq \varphi \leq d_1$. Thus,

$$V_{bat}d_2T + (V_{bat} - u_{c1})\varphi T + (V_{bat} - u_o)(1 - d_2 - \varphi)T = 0 \quad (13)$$

$$V_{fc}d_1T + (V_{fc} + u_{c1} - u_o)(1 - d_1)T = 0 \quad (14)$$

the voltage across capacitor C_1 and the output can be derived from Equations (9) and (10) as follows.

$$u_{c1} = \frac{V_{bat} - (1 - d_2 - \varphi)u_o}{\varphi} \quad (15)$$

$$u_o = \frac{\varphi}{(1 - d_1)(1 - d_2)}V_{fc} + \frac{1}{1 - d_2}V_{bat} \quad (16)$$

Similar to condition 2 above, when $d_1 + d_2 < 1$ and $d_1 < d_2$, then $0 < \varphi \leq d_1$. The volt-second balance analysis of the inductors L_1 and L_2 is the same as Equations (9) and (10) under this condition, and the voltage across capacitor C_1 and the output are the same as Equations (11) and (12). As $\varphi = 0$, battery supplies power to load directly, and the volt-second balance analysis is shown below.

$$V_{bat}d_2T + (V_{bat} - u_o)(1 - d_2)T = 0 \quad (17)$$

$$V_{fc}d_1T + (V_{fc} + u_{c1} - u_o)(1 - d_1)T = 0 \quad (18)$$

the voltage across capacitor C_1 and the output can be derived from Equations (13) and (14) as follows.

$$u_{c1} = \frac{(1 - d_1)u_o - V_{fc}}{(1 - d_1)} \quad (19)$$

$$u_o = \frac{1}{1 - d_2}V_{bat} \quad (20)$$

The above Equations (12), (16) and (20) show the calculation formula and control method of energy distribution for this topology. Analyzing the ideal state of $d_1 + d_2 \geq 1$, Equation (12) is multiplied by the output current I_o and the respective input power of the fuel cell and the battery can be known, which will be explained later.

3.1.4. State 4

The input voltage in this state is V_{fc} , while the output is V_{bat} and u_o , and the duty cycles of switches S1, S2, and S5 are d_1 , d_2 , and d_5 , of which S1 and S5 are in complementary conduction such that $d_1 + d_5 = 1$. When S5 is on, the capacitor C_1 and the load R_o will form a parallel connection, the battery discharges to the capacitor and load, then $u_o = u_{c1} + V_{bat}$, by applying the volt-second balance law over the inductors L_1 and L_2 , we have:

$$(V_{fc} - u_{c1})d_1T + (V_{fc} - u_{c1} - V_{bat})(d_5 - d_2)T + V_{fc}d_2T = 0 \quad (21)$$

$$V_{fc}d_1T + (V_{fc} - V_{bat})(d_5 - d_2)T + (V_{fc} - V_{bat})d_2T = 0 \quad (22)$$

the voltage across capacitor C_1 and the output of the battery and load port can be derived from Equations (21) and (22) as follows.

$$u_{c1} = \frac{d_2}{d_5(1 - d_2)}V_{fc} \quad (23)$$

$$V_{bat} = \frac{1}{d_5}V_{fc} \quad (24)$$

$$u_o = u_{c1} + V_{bat} = \frac{1}{d_5(1 - d_2)}V_{fc} \quad (25)$$

3.1.5. State 5

The load feedback voltage is u_o , the battery's energy-storage port voltage is V_{bat} , and the duty cycle of switch S4 is d_4 , by applying the volt-second balance law over the inductors L_1 and L_2 , we have:

$$(u_o - V_{bat})d_4T - V_{bat}(1 - d_4)T = 0 \quad (26)$$

the transformer voltage relationship is simply shown below.

$$V_{bat} = \frac{1}{d_4}u_o \quad (27)$$

3.2. Switching Capacitor Charge/Discharge Characteristics Analysis

Taking state 1 as an example, the equivalent circuit for the capacitor charging and discharging is shown in Figure 3.

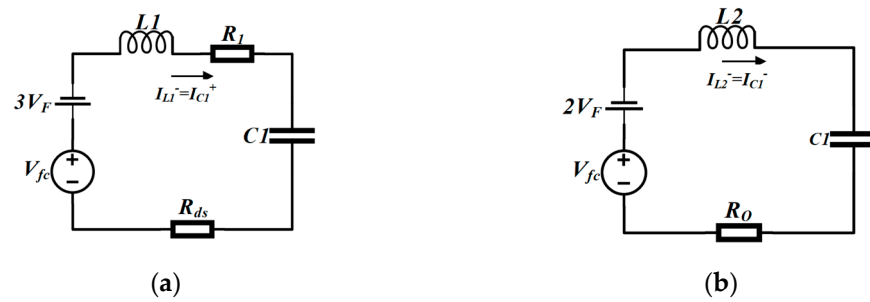


Figure 3. The equivalent circuit for capacitor charging and discharging: (a) charging circuit; (b) discharging circuit.

In Figure 3, R_{ds} is the on-resistance of switch S1, V_F is the on-voltage drop of diode, the inductor and capacitor internal resistance is much smaller than the equivalent load R_o , and R_1 is the NTC thermistor. If the inductor and capacitor internal resistance is ignored, the voltage ripple coefficient of the switching capacitor is analyzed as follows.

According to the relationship between the capacitor voltage and current:

$$C_1 \frac{du_{c1}}{dt} = i_{c1} \tag{28}$$

since the inductor current is constant over the period, the value of the change in inductor current is $\Delta i_{L1}^+ = \Delta i_{L1}^-$. Obviously, the current of capacitor C_1 in Figure 3 is Δi_{L1}^+ or Δi_{L1}^- , as follows:

$$i_{c1}^+ = \Delta i_{L1}^- = \frac{1}{L_1} (V_{fc} - 3V_F - u_{c1} - \Delta i_{L1}^- R_1) (1 - d_2) T = \Delta i_{L1}^+ = \frac{1}{L_1} (V_{fc} - 2V_F) d_2 T \tag{29}$$

substituting Equation (29) into Equation (28) yields the capacitor voltage ripple as:

$$\Delta u_{c1} = \frac{1}{C_1 L_1} (V_{fc} - 2V_F) d_2 T \tag{30}$$

the ripple coefficient γ is:

$$\gamma = \frac{\Delta u_{c1}}{V_{fc}} = \frac{1}{V_{fc} C_1 L_1} (V_{fc} - 2V_F) d_2 T \tag{31}$$

As can be seen from Equation (31), the larger the duty cycle and switching period, the larger the γ , while the larger the inductance and capacitance values, the smaller the γ .

Because of the mismatch of the voltage between the input and capacitor, another NTC resistor is connected in the series circuit, then the resonant spike current that appears in the capacitor at the moment of conduction is calculated as follows.

$$i = \frac{I_{fcint} Z_n + V_{fc} \sin \omega_n t}{Z_n + R_1 \sin \omega_n t} (t \rightarrow 0^+) \tag{32}$$

where $Z_n = \sqrt{L_1/C_1}$ is the inductor-capacitor series characteristic impedance, $\omega_n = 1/\sqrt{L_1/C_1}$ is the series resonant frequency. Apparently, when the resistance R_1 is zero, the starting current approach to the initial current of inductor discharging I_{fcint} at t tends to be zero.

3.3. Voltage and Current Analysis

Analyzing various equivalent circuits, we can obtain the voltage stress of switches S1–S6 and diodes D1–D5 as:

$$\begin{cases} u_{s1} = u_{D2} = u_o - u_{c1} \\ u_{s2} = u_{c1} \\ u_{s3} = u_b - u_{fc} \\ u_{s4} = u_{D4} = u_o - u_b \\ u_{s5} = u_{D5} = u_b \end{cases} \quad (33)$$

according to the input-output gain relationship derived from Section 2.2, combined with the power conservation theorem, the following conclusions can be easily deduced.

- The average current of inductors is equal at state 1 and state 2, and the sum of the two is equal to the input current I_{in} . The system does not carry out power distribution at this time, thus:

$$I_{L1} = I_{L2} = \frac{1}{2}I_{in} = \frac{1}{2} \frac{2}{(1-D)} I_o \quad (34)$$

where I_{in} can be the input current of the fuel cell or battery, and D is the duty cycle of switches S1 and S2.

- Similarly, I_{L1} and I_{L2} are equal to the battery input current I_b and fuel cell input current I_{fc} , respectively, at state 3, so:

$$I_{L1} = I_b = \frac{1}{(1-d_2)} I_o \quad (35)$$

$$I_{L2} = I_{fc} = \frac{1}{(1-d_1)} I_o \quad (36)$$

or

$$I_{L2} = I_{fc} = \frac{\varphi}{(1-d_1)(1-d_2)} I_o \quad (37)$$

- As mentioned before, the average current I_{L1} and I_{L2} is equal to the fuel cell input current I_{fc1} and I_{fc2} at state 4, so:

$$I_{L1} = I_{fc1} = \frac{1}{(1-d_2)d_5} I_o \quad (38)$$

$$I_{L2} = I_{fc2} = \frac{1}{d_5} I_b \quad (39)$$

- When braking feedback, the average current I_{L3} of inductor I_{L3} is equal to the output current I_b , thus we can obtain:

$$I_{L3} = I_b = \frac{1}{d_4} I_{Load} \quad (40)$$

where I_{Load} is the braking feedback current.

4. Topology Dynamic Modeling and Controller Solutions

The improved converter topology can work in five operating states, and each of them corresponds to a different power output requirement. In states 1 and 2, the system does not perform power distribution, so only the output voltage is controlled. In state 3, it is necessary to control the voltage of the output and capacitor C1, thereby controlling the power input of the different ports. In state 4, the output of the load and battery port needs to be controlled, which can be achieved by adjusting the voltage of capacitor C1. In state 5, only the battery port voltage needs to be controlled.

Based on the above output requirements, the mathematical model of the topology is analyzed. As described previously in Section 2.1, since the structure of models 1 to 4 is similar, let the current through the inductors L_1 and L_2 and the voltage across the capacitors C_1 and C_o be the state variables $\hat{x}_{1,2,3,4}$. Furthermore, let the duty cycle d_1 and d_2 be the control variables $\hat{u}_{1,2,3,4}$. For state 5, set the current of the inductor L_3 and the voltage of the capacitor C_b at the battery end as state variables \hat{x}_5 , and the duty cycle d_4 as the control variables \hat{u}_5 .

In addition, let R_o and R_b be the load and battery port equivalent resistance in known conditions. Finally, five different state space averaging models can be derived as follows.

State 1: switches S1 and S2 have an equal duty cycle $d_1 = d_2 = D$ in this state to control the output voltage U_o , its state-space expression is:

$$\begin{cases} L_1 \frac{di_{L1}}{dt} = V_{fc} - (1 - D)(u_{fc} + i_{L1}R_1) \\ L_2 \frac{di_{L2}}{dt} = V_{fc} + (1 - D)(u_{c1} - u_o) \\ C_1 \frac{du_{C1}}{dt} = (1 - D)i_{L1} - (1 - D)i_{L2} \\ C_o \frac{du_{C_o}}{dt} = (1 - D)i_{L2} - \frac{u_o}{R_o} \end{cases} \quad (41)$$

State 2: as in 1, the input voltage is changed. Its state-space expression is,

$$\begin{cases} L_1 \frac{di_{L1}}{dt} = V_{bat} - (1 - D)(u_{fc} + i_{L1}R_1) \\ L_2 \frac{di_{L2}}{dt} = V_{bat} + (1 - D)(u_{c1} - u_o) \\ C_1 \frac{du_{C1}}{dt} = (1 - D)i_{L1} - (1 - D)i_{L2} \\ C_o \frac{du_{C_o}}{dt} = (1 - D)i_{L2} - \frac{u_o}{R_o} \end{cases} \quad (42)$$

State 3: the duty cycle d_1 and d_2 control the output voltage U_o and Capacitance voltage U_{c1} . Its state-space expression is:

$$\begin{cases} L_1 \frac{di_{L1}}{dt} = V_{bat} - (1 - d_2)(u_{fc} + i_{L1}R_1) \\ L_2 \frac{di_{L2}}{dt} = V_{fc} + (1 - d_1)(u_{c1} - u_o) \\ C_1 \frac{du_{C1}}{dt} = (1 - d_2)i_{L1} - (1 - d_1)i_{L2} \\ C_o \frac{du_{C_o}}{dt} = (1 - d_1)i_{L2} - \frac{u_o}{R_o} \end{cases} \quad (43)$$

State 4: the duty cycle d_1 and d_2 control the output voltage U_o and Capacitance voltage U_{c1} and then the battery port voltage V_{bat} will be uniquely determined by the former. Its state-space expression is:

$$\begin{cases} L_1 \frac{di_{L1}}{dt} = V_{fc} - (1 - d_1 - d_2)u_o - d_1u_{c1} - (1 - d_2)i_{L1}R_1 \\ L_2 \frac{di_{L2}}{dt} = V_{fc} + (1 - d_1)(u_{c1} - u_o) \\ C_1 \frac{du_{C1}}{dt} = (1 - d_2)i_{L1} - d_2(i_{L2} - \frac{u_o}{R_{bat}} + \frac{u_{c1}}{R_{bat}}) \\ C_o \frac{du_{C_o}}{dt} = d_2(i_{L2} - \frac{u_o}{R_{bat}} + \frac{u_{c1}}{R_{bat}}) - \frac{u_o}{R_o} \end{cases} \quad (44)$$

State 5:

$$\begin{cases} L_3 \frac{di_{L3}}{dt} = d_4(u_o - V_{bat}) - (1 - d_4)V_{bat} \\ C_b \frac{dV_{bat}}{dt} = d_4i_{L3} - \frac{V_{bat}}{R_{bat}} \end{cases} \quad (45)$$

Based on the small-signal modeling approach [31,32], the state variables \hat{x} , control variables \hat{u} , and input variables \hat{v} in Equations (41)–(45) contain stable values $\hat{X}, \hat{U}, \hat{V}$ and small-signal perturbations $\hat{\tilde{x}}, \hat{\tilde{u}}, \hat{\tilde{v}}$. Assuming that the perturbation is much smaller than the stability term in one cycle, the matrix form of the small signal model is obtained by substituting it into expressions (41) to (45) and neglecting its second-order term as follows:

States 1 and 2:

$$A = \begin{bmatrix} -\frac{R_1}{L_1}(1-D) & 0 & -\frac{(1-D)}{L_1} & 0 \\ 0 & 0 & \frac{1-D}{L_2} & -\frac{1-D}{L_2} \\ \frac{1-D}{C_1} & -\frac{1-D}{C_1} & 0 & 0 \\ 0 & \frac{1-D}{C_o} & 0 & 0 \end{bmatrix}, \tilde{x} = \begin{bmatrix} \tilde{i}_{L1} \\ \tilde{i}_{L2} \\ \tilde{u}_{c1} \\ \tilde{u}_o \end{bmatrix}, B = \begin{bmatrix} U_{c1} + I_{L1}R_1 \\ U_o - U_{c1} \\ I_{L2} - I_{L1} \\ -I_{L2} \end{bmatrix}, \tilde{u} = \tilde{d}, C = \begin{bmatrix} 0 & 0 & 0 & 0 \\ 0 & 1 & 0 & 0 \\ 0 & 0 & 0 & 0 \\ 0 & 0 & 0 & 1 \end{bmatrix} \quad (46)$$

State 3:

$$A = \begin{bmatrix} -\frac{R_1}{L_1}(1-D_2) & 0 & -\frac{(1-D_2)}{L_1} & 0 \\ 0 & 0 & \frac{1-D_1}{L_2} & -\frac{1-D_1}{L_2} \\ \frac{1-D_2}{C_1} & -\frac{1-D_1}{C_1} & 0 & 0 \\ 0 & \frac{1-D_1}{C_o} & 0 & 0 \end{bmatrix}, \tilde{x} = \begin{bmatrix} \tilde{i}_{L1} \\ \tilde{i}_{L2} \\ \tilde{u}_{c1} \\ \tilde{u}_o \end{bmatrix}, B = \begin{bmatrix} 0 & U_{c1} + I_{L1}R_1 \\ U_o - U_{c1} & 0 \\ I_{L2} & -I_{L1} \\ -I_{L2} & 0 \end{bmatrix}, \tilde{u} = \begin{bmatrix} \tilde{d}_1 \\ \tilde{d}_2 \end{bmatrix} \quad (47)$$

$$C = \begin{bmatrix} 0 & 0 & 0 & 0 \\ 0 & 1 & 0 & 0 \\ 0 & 0 & 1 & 0 \\ 0 & 0 & 0 & 1 \end{bmatrix}.$$

State 4:

$$A = \begin{bmatrix} -\frac{R_1}{L_1}(1-D_2) & 0 & -\frac{D_1}{L_1} & -\frac{(1-D_1-D_2)}{L_1} \\ 0 & 0 & \frac{1-D_1}{L_2} & -\frac{1-D_1}{L_2} \\ \frac{1-D_2}{C_1} & -\frac{D_2}{C_1} & 0 & 0 \\ D_2 & 0 & 0 & 0 \end{bmatrix}, \tilde{x} = \begin{bmatrix} \tilde{i}_{L1} \\ \tilde{i}_{L2} \\ \tilde{u}_{c1} \\ \tilde{u}_o \end{bmatrix}, B = \begin{bmatrix} U_o - U_{c1} & U_o + I_{L1}R_1 \\ -U_o & U_{c1} \\ 0 & \frac{U_o - U_{c1}}{R_{bat}} - I_{L1} - I_{L2} \\ 0 & I_{L1} - \frac{U_o - U_{c1}}{R_{bat}} \end{bmatrix}, \quad (48)$$

$$\tilde{u} = \begin{bmatrix} \tilde{d}_1 \\ \tilde{d}_2 \end{bmatrix}, C = \begin{bmatrix} 0 & 0 & 0 & 0 \\ 0 & 1 & 0 & 0 \\ 0 & 0 & 1 & 0 \\ 0 & 0 & 0 & 1 \end{bmatrix}$$

State 5:

$$A = \begin{bmatrix} 0 & -1 \\ D_4 & 0 \end{bmatrix}, \tilde{x} = \begin{bmatrix} \tilde{i}_{L3} \\ \tilde{u}_{bat} \end{bmatrix}, B = \begin{bmatrix} D_4 & U_o \\ 0 & I_{L3} \end{bmatrix}, \tilde{u} = \begin{bmatrix} \tilde{u}_o \\ \tilde{d}_4 \end{bmatrix}, C = [0 \quad 1] \quad (49)$$

In summary, this paper discusses the corresponding small-signal models for the five states, and then the system transfer function can be derived to analyze the closed-loop control method.

In designing the controller, a proportional-integral controller is used to eliminate the steady-state error of the system and improve the dynamic following performance of the system.

It is important to emphasize that, due to the discharge characteristics of the fuel cell itself, the topology requires that the power input be able to be changed in time to meet the load demands and protect the fuel cell. Therefore, in state 3, the topology will make the input power P_{fc} proportional to P_{bat} according to the energy management strategy. According to Equations (11), (12), (35) and (36), this proportional relationship is expressed as $P_{fc}:P_{bat} = (U_o - U_{c1}):U_{c1}$. Therefore, the control volume also needs to control the relationship between the magnitude of the load output and the capacitor C1 voltage to regulate the proportion of power input.

Figure 4 shows the control block diagram for system state 1 to 5. The error value is used as the input to the PI controller, and the PI controller output is limited by the saturation module, which subsequently controls the PWM waves.

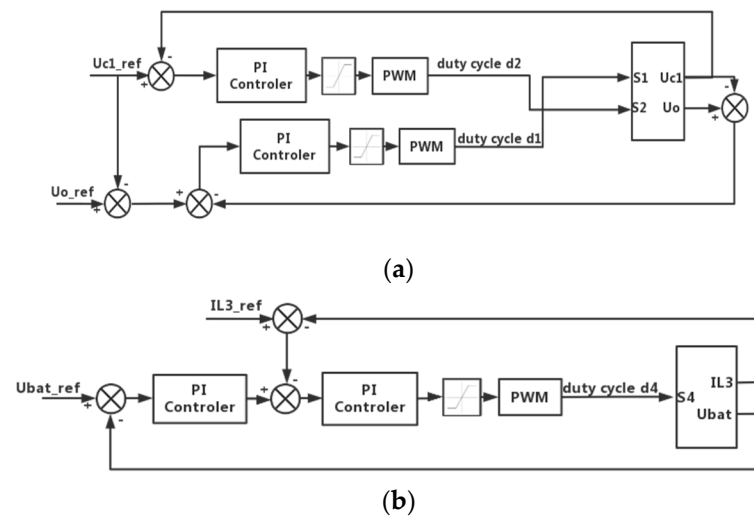
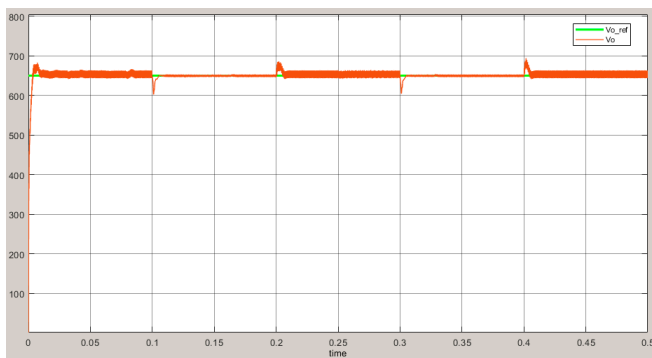
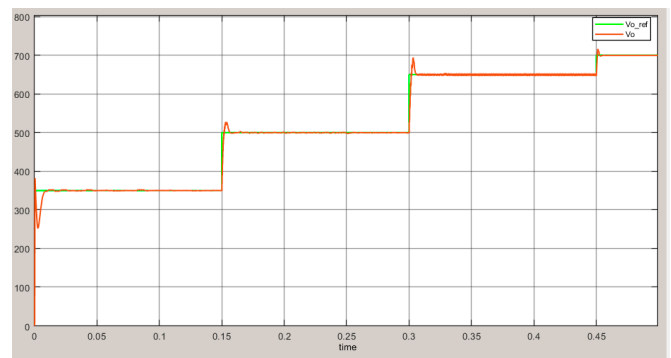


Figure 4. System control block diagram: (a) control block diagram of state 1 to 4 ($d_1 = d_2$ at state 1 and 2, $d_1 \neq d_2$ at state 3 and 4); (b) control block diagram of state 5.

The following image is derived from Matlab/simulink software, which shows the output waveform of the system after adding PI control. When the topology is working in state 1 or 2, Figure 5a shows the process of output voltage stabilization when the topology repeatedly switches loads, and Figure 5b shows the performance of the output voltage following the desired value.



(a)



(b)

Figure 5. The effect of controller under working state 1 and 2: (a) output voltage under load switching conditions; (b) output voltage following the desired value schematic.

When the topology is operating in state 3, Figure 6a shows the process of output voltage stabilization when changing the voltage proportionality ($U_o - U_{c1}$): U_{c1} . Then, Figure 6b shows the effect of changing the ratio of the two energy power inputs with the desired voltage ratio. The control principle of state 4 does not differ from state 3, so it is not repeated.

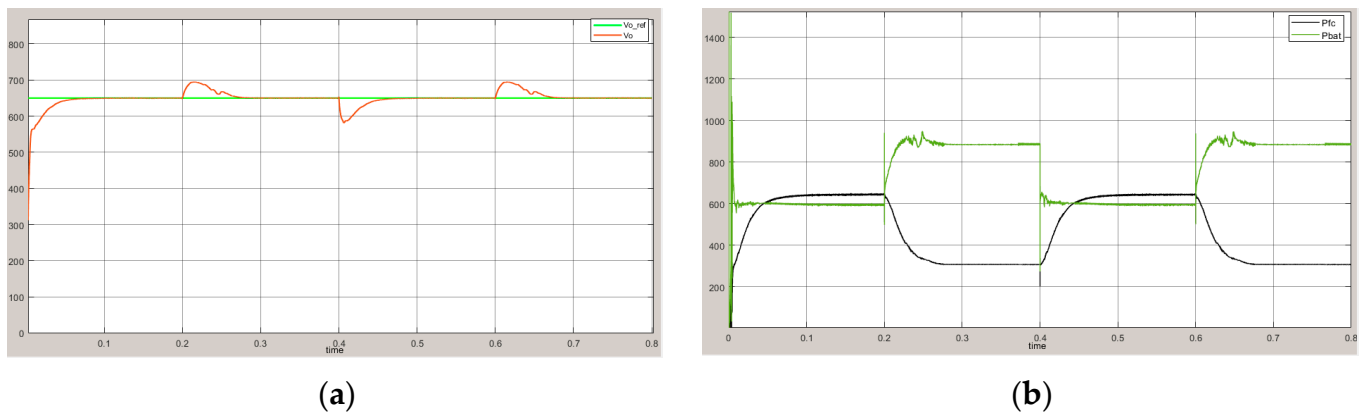


Figure 6. The effect of controller under working state 3: (a) output voltage under variable voltage scaling conditions; (b) result of proportional change in power input.

When the topology is operating in state 5, Figure 7 shows a schematic diagram of the battery port maintaining a constant voltage when the load feedback voltage varies depending on the braking effect.

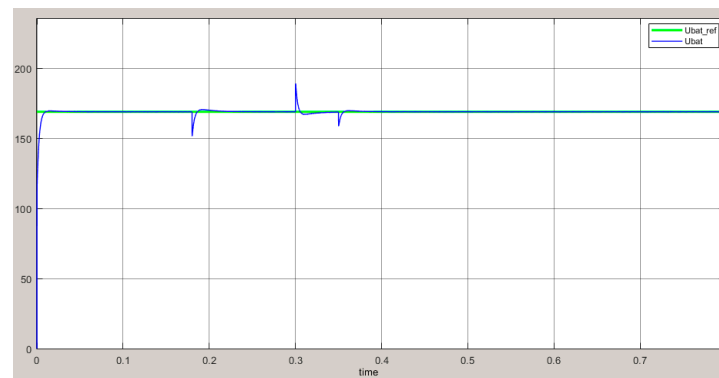


Figure 7. Output results for variable input voltage at operating state 5.

It can be expected that the converter system with proportional-integral control has significantly improved stability and dynamic performance.

5. Comparative Analysis of Related Converter Topologies

In this paper, the proposed integrated converter for fuel cell hybrid vehicles is compared with other on-board multi-port converters, and the converter performance is summarized, as shown in Table 1. Taken from the power level, only the study by [11] and this paper are designed by 1 kw power, the others are small power. In terms of whether the energy ports can operate independently, the converter topology ports proposed in the literature [11,14,24] fail to meet the requirements. In terms of the power distribution capability, only this paper and the literature [11,28] have studied the design of power distribution program for hybrid vehicles. Most importantly, only this paper and the literature [11,14,16] have the capability of bidirectional transformation.

Table 1. Comparison of the proposed integrated converter topology with other on-board converters.

Study Number	Number of Switches	Number of Inductors	Number of Capacitors	Boost Gain	Number of Applicable States	Bi-Directional Function	Power Distribution Function	Port Independently
[11]	4	2	1	$\frac{d_2}{1-d_1}$	3	✓	✓	×
[14]	3	2	3	$\frac{1+D}{1-D}V_L + V_2$	2	✓	×	×
[16]	3	2	3	$\frac{1}{1-d_1}$	5	✓	×	✓
[24]	4	2	1	$\frac{(1+D^2-d)}{(1-D)^2}$	3	×	×	×
[27]	3	3	3	$1 + \frac{1}{1-D}$	5	×	×	✓
[28]	5	2	2	$\frac{2}{1-D}$	4	×	✓	✓
Proposed	6	3	2	$\frac{2}{1-D}$	5	✓	✓	✓

The number of switches in the integrated converter topology of the fuel cell hybrid vehicle proposed in this paper is only one more than that of the literature [28], and the number of switching devices and magnetic devices are also less than that of a general isolated converter. At the same time, the topology has a higher power level and bidirectional characteristics, and also has more applicable operating conditions, higher gain output, and can meet the hybrid energy power distribution task better than the general on-board non-isolated converter. These advantages make it one of the best solutions for on-board converters for hybrid vehicles, especially for fuel cell hybrids.

6. Simulation Experiments and Results Analysis

In this section, the genuine matlab/simulink simulation software is used to verify the steady-state and voltage-current analyses presented in the previous section, and the experimental parameters of the simulation model are shown in Table 2.

Table 2. Experimental parameters of the simulation model.

Parameters	Values	Parameters	Values
Fuel cell voltage V_{fc}	120 to 160 V	Inductor L_1	1.28×10^{-3} H
Battery voltage V_{bat}	168 V	Inductor L_2	1.28×10^{-3} H
Load rated voltage u_o	650 V	Inductor L_3	0.747×10^{-3} H
Load port current I_o	1.5 A	Capacitor C_1	4.8×10^{-6} F
Battery port resistance R_{bat}	25 Ω	Capacitor C_o	9.192×10^{-6} F
Load port resistance R_o	422 Ω	Frequency	100 kHz

The switch conduction is first simulated to verify the equivalent circuit output results for each state of operation. Figure 8 demonstrates the simulation results when operating in state 1 and state 2. Figure 8a shows the voltages of output and capacitor, and Figure 8b shows the average currents and their waveform of inductors L_1 and L_2 , when the input is fuel cell. While Figure 8c,d shows the same items when the input is the battery.

Figure 9 shows the simulation results when operating in state 3. In this state, the duty cycle is adjusted to different values so that the energy provided by both energy ports is proportional to the other. Figure 9a shows the voltages of the output and capacitor, and Figure 9b shows the average currents and their waveform of inductors L_1 and L_2 at this time.

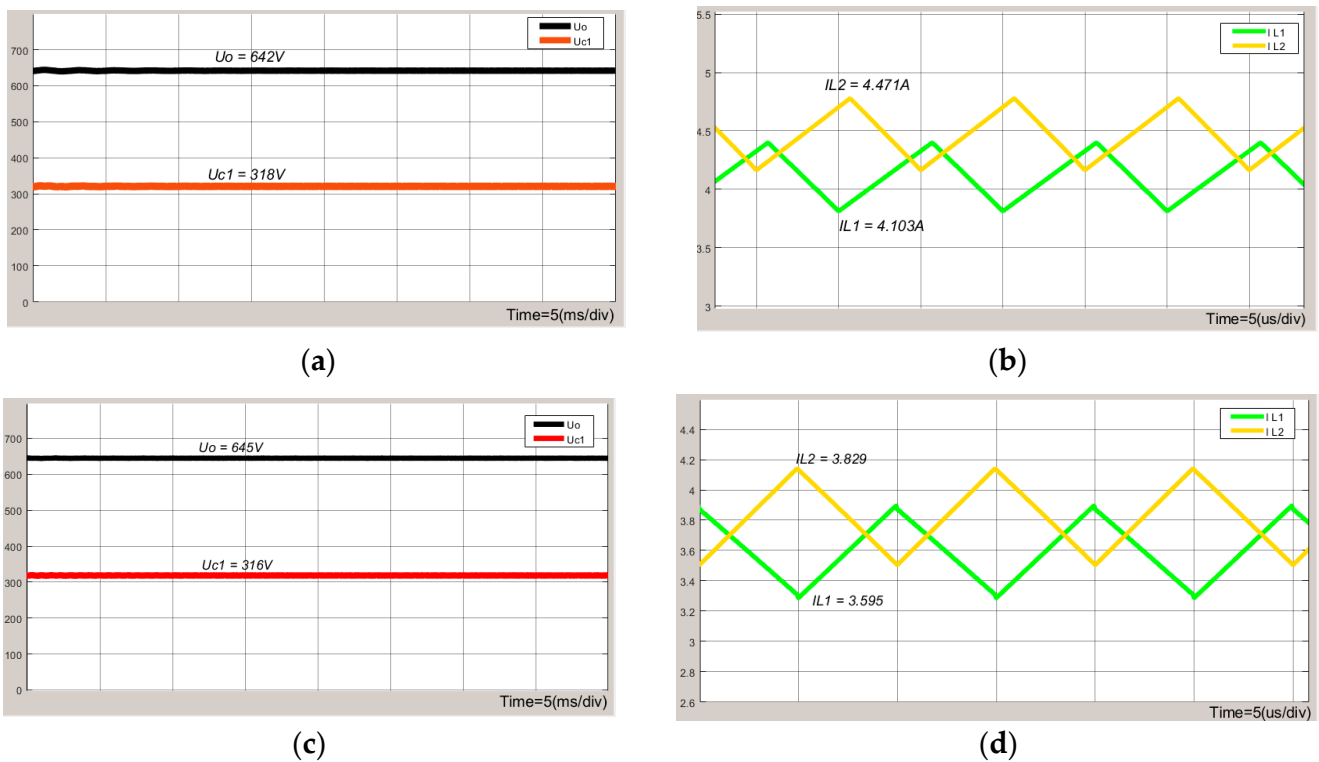


Figure 8. The simulation results of state 1 and 2: (a) the voltages of output and capacitor in state 1; (b) the average currents and their waveforms of inductors L_1 and L_2 in state 1; (c) the voltages of output and capacitor in state 2; (d) the average currents and their waveforms of inductors L_1 and L_2 in state 2.

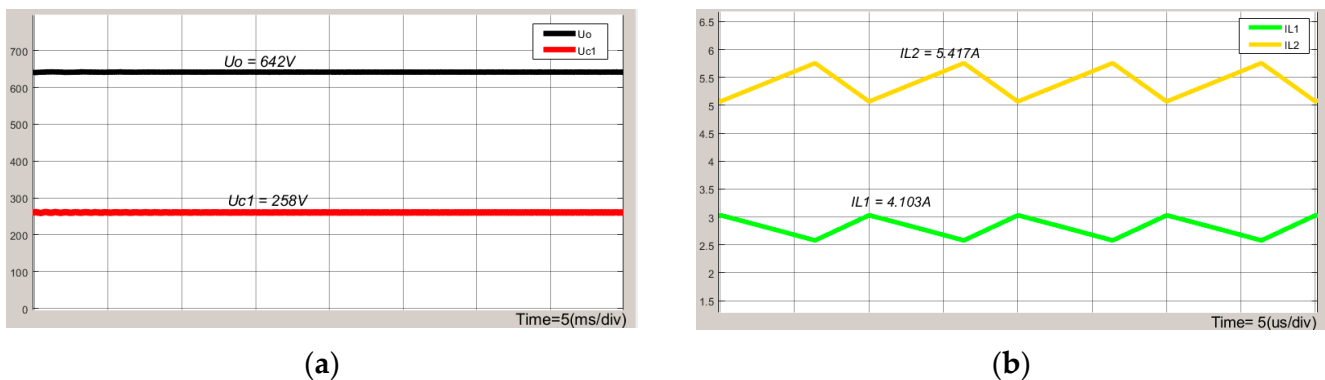


Figure 9. The simulation results of state 3: (a) the voltages of output and capacitor in state 3; (b) the average currents and their waveforms of inductors L_1 and L_2 in state 3.

Figure 10 shows the simulation results in state 4; at this time, the DC voltage source at the battery port is replaced with a 25Ω resistor. Where Figure 10a shows the waveform of the battery port, output port, and capacitor voltage, and Figure 10b shows the average currents and their waveform of inductors L_1 and L_2 and battery port at this time. The battery port is kept at a constant voltage in this operating mode.

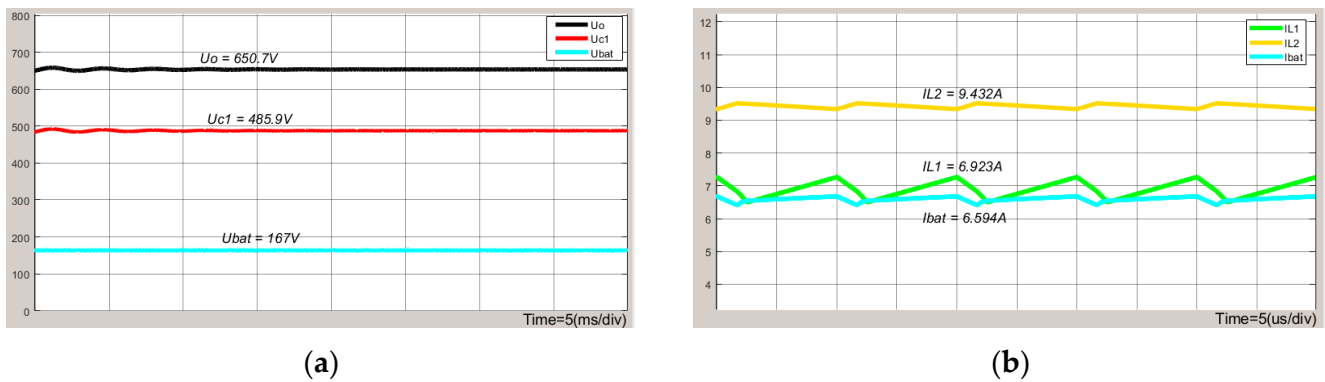


Figure 10. The simulation results of charging work: (a) the load and battery output voltage in state 4; (b) the average currents and waveforms in state 4.

Figure 11 shows the simulation results in state 5; similarly, the DC voltage source at the battery port is replaced with a 25Ω load resistor, while the resistor at the load port is replaced with a DC power supply. Figure 11a shows the charging voltage when the battery port is used as a load, and Figure 11b shows the average value of the inductor L_3 current and the charging and discharging waveform.

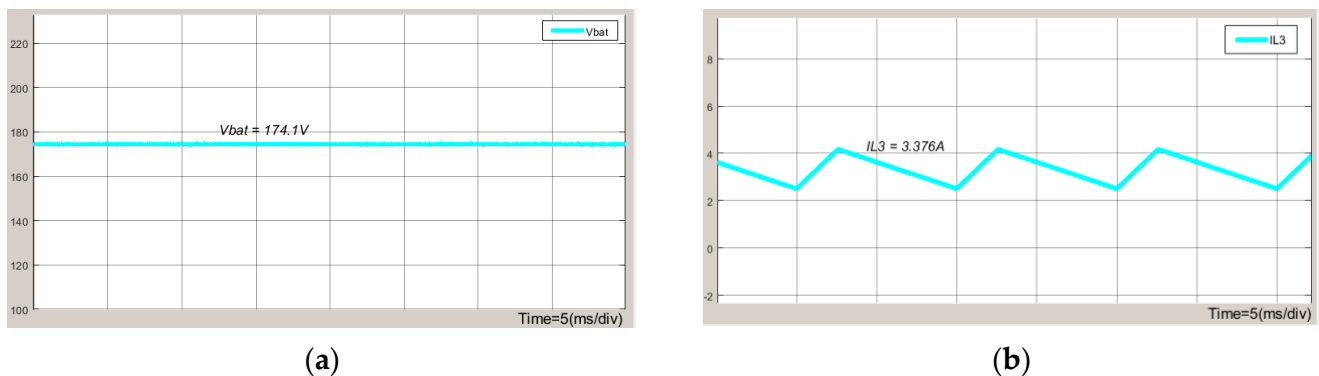


Figure 11. The simulation results of the operation of the load braking energy feedback: (a) the battery charging voltage in state 5; (b) the inductance current in state 5.

The above simulation experimental results show that the steady-state gain of the system, the distribution ratio of input energy, and the waveform of device charging and discharging are roughly in line with the theoretical calculation, and the topology can operate in CCM mode, and the bidirectional conversion capability is verified.

The current spike of the capacitor in the simulation mode is caused by the mismatch between the input and capacitor. Without the NTC module, the charging current is visible, as shown in Figure 12a, with an inrush current of about 40A present during initial time. After adding the NTC module, the charging current of the simulation model is shown in Figure 12b, and it can be seen that the spike current appearing in the capacitor at the moment of starting is significantly reduced by twice. As the simulation time increases, the capacitor is charged to a stable voltage value and the voltage mismatch is eliminated, also verifying the reliability of the topology at steady state.

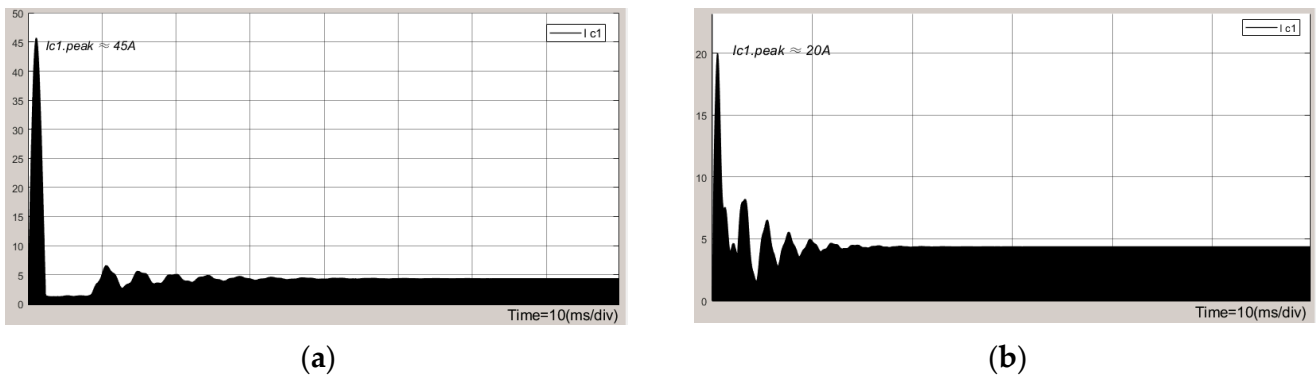


Figure 12. Capacitor charging spike current waveform: (a) current without thermistor in series; (b) current with thermistor in series.

This paper establishes a state selector model based on simulation time, which changes the duty cycle of the topology’s switch according to the time order, and Figure 13 shows the simulation output results of topology in states 1 to 4. Figure 13a,b shows the output voltage and current waveform under state selector control, respectively. The output voltage can output a sTable 650 V to load bus. In addition, the state selection sequence is shown in Figure 13c, which simulates the actual operation of the fuel cell hybrid vehicle. Figure 14 illustrates the battery port voltage waveform corresponding to Figure 13.

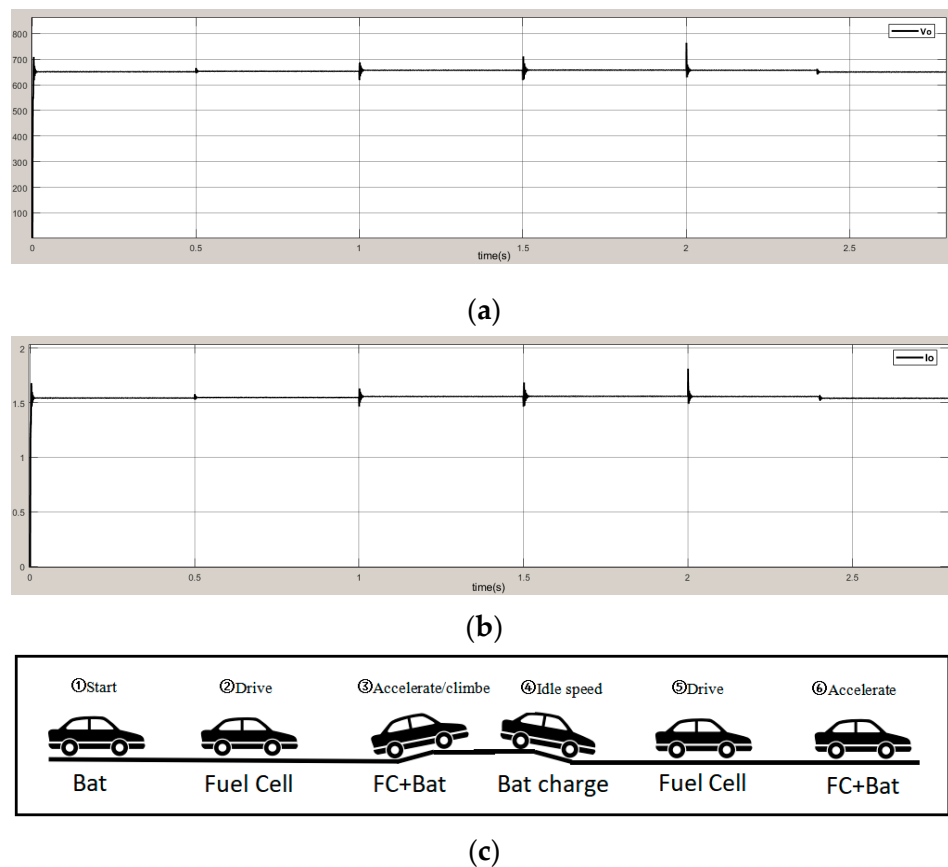


Figure 13. The output during state switching and its sequence: (a) voltage waveform of operating state switching; (b) current waveform of operating state switching; (c) switching sequence of operating states.

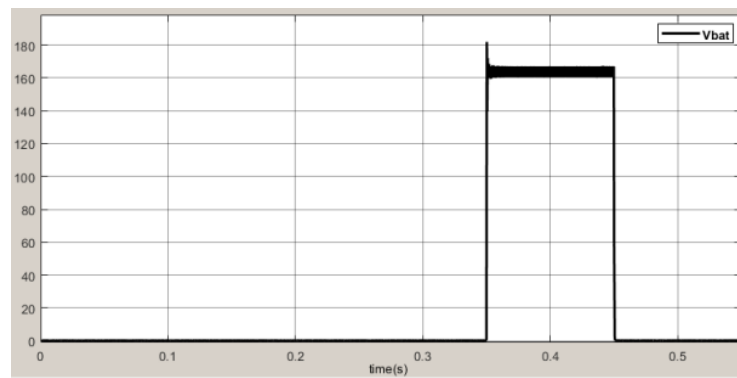


Figure 14. Charging voltage of battery port.

Figure 15 shows the simulation waveform of the battery port charged by the voltage source of the load port when state 5 is selected.

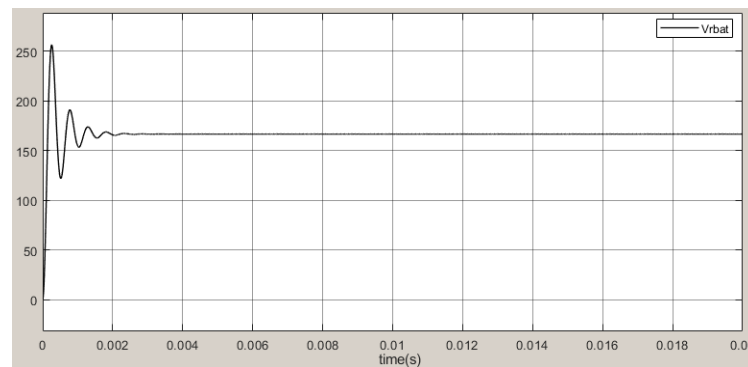


Figure 15. Charging voltage of battery port in feedback state.

Figure 16 shows the output efficiency of the load bus for each operating mode of the topology, as seen in the high power application scenario still has an output efficiency of more than 80%.

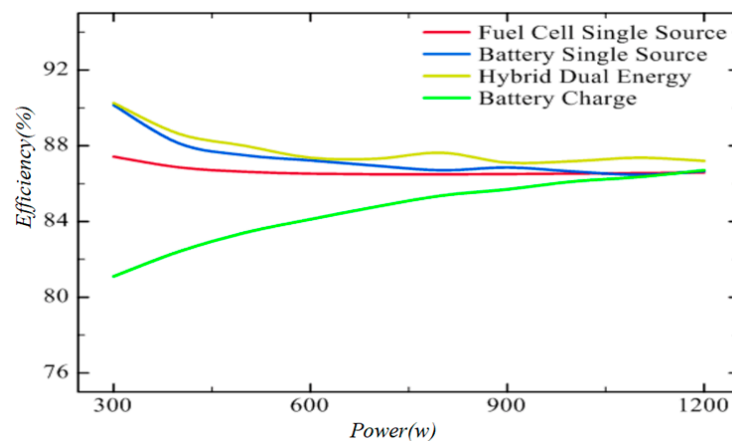


Figure 16. Output efficiency in each state.

Finally, the simulation results show that the output waveform is basically stable and can meet the driving requirements of the fuel cell hybrid vehicle.

7. Conclusions

In this paper, an integrated converter for hybrid vehicles is proposed. By upgrading the non-isolated three-port topology, the proposed converter possesses high-gain output and solves the problem of charging rises of the switching capacitor as a voltage doubling unit. The use of non-isolated topology can avoid the severe magnetic losses of converter and, simultaneously, can effectively ameliorate the power density of the system.

Evidently, the proposed integrated converter topology not only has the bidirectional conversion function, but also can regulate the proportional relationship of the input energy under the control of a sensible power distribution strategy, i.e., it can improve the efficient utilization rate of hybrid energy, which is suitable for most of the driving conditions of hybrid vehicles. The experimental results further validate steady-state analyses in this paper and illustrate the feasibility of topology.

This paper provides a reliable solution for using highly integrated converters in industrial and automotive applications.

Author Contributions: Conceptualization, W.L. and W.X.; methodology, W.X.; software, W.X.; validation, W.X.; formal analysis, all authors; investigation, all authors; writing—original draft preparation, W.L.; writing—review and editing, Y.Q. and W.L.; visualization, W.X.; project administration, W.L. and Y.Q.; funding acquisition, W.L. and Y.Q. All authors have read and agreed to the published version of the manuscript.

Funding: This research was funded by the National Natural Science Foundation of China, grant number 61563006; and the Independent Research Project of Guangxi Key Laboratory of Auto Parts and Vehicle Technology, grant number 2020GKLACVTZZ02.

Data Availability Statement: Not applicable.

Acknowledgments: The authors would like to thank all the anonymous reviewers for their insightful comments and constructive suggestions.

Conflicts of Interest: The authors declare no conflict of interest.

References

1. Gao, Z.; Li, X.; Liu, Z.; Rao, J. Research status and development trend of hydrogen fuel cell vehicles. *Mater. Rep.* **2022**, *36*, 74–81. [[CrossRef](#)]
2. Guo, N.; Zhang, X.; Zou, Y.; Guo, L.; Du, G. Real-time predictive energy management of plug-in hybrid electric vehicles for coordination of fuel economy and battery degradation. *Energy* **2021**, *214*, 119070. [[CrossRef](#)]
3. Feng, Y. Toyota Mirai hydrogen fuel cell vehicle analysis. *Automot. Repair Maint.* **2020**, *8*, 71–73.
4. Babaei, E.; Sakhavati, S. An overview of different topologies of multi-port dc/dc converters for dc renewable energy source applications. In Proceedings of the 2016 13th International Conference on Electrical Engineering/Electronics, Computer, Telecommunications and Information Technology, Chiang Mai, Thailand, 28 June–1 July 2016. [[CrossRef](#)]
5. Vermulst, B.J.; Duarte, J.L.; Lomonova, E.A.; Wijnands, K.G. Scalable multi-port active-bridge converters: Modelling and optimised control. *IET Power Electron.* **2017**, *10*, 80–91. [[CrossRef](#)]
6. Song, S.; Li, W.; Ni, K.; Xu, H.; Hu, Y.; Si, J. Modular Multi-Port Ultra-High Power Level Power Converter Integrated with Energy Storage for High Voltage Direct Current (HVDC) Transmission. *Energies* **2018**, *11*, 2711. [[CrossRef](#)]
7. Wang, C.; Li, W.; Wang, Y.; Han, F.; Meng, Z.; Li, G. An Isolated Three-Port Bidirectional DC-DC Converter with Enlarged ZVS Region for HESS Applications in DC Microgrids. *Energies* **2017**, *10*, 446. [[CrossRef](#)]
8. Li, W.; Wang, Y.; Han, F.; Chen, B. An isolated three-port bidirectional LCLC multiresonant DC converter. *Trans. China Electrotech. Soc.* **2018**, *33*, 3231–3244. [[CrossRef](#)]
9. Peng, Y. Study of Input-Output Relationships of Four-Port DC Converters. *Chin. LABAT Man* **2018**, *55*, 18–22. [[CrossRef](#)]
10. Wang, H.; Li, H.; Liu, J. A Wide-Range Soft-Switching High-Gain Bidirectional Multi-Port Converter. *Power Electron.* **2019**, *53*, 74–77+82.
11. Akar, F.; Tavlasoglu, Y.; Ugur, E.; Vural, B.; Aksoy, I. A Bidirectional Nonisolated Multi-Input DC–DC Converter for Hybrid Energy Storage Systems in Electric Vehicles. *IEEE Trans. Veh. Technol.* **2016**, *65*, 7944–7955. [[CrossRef](#)]
12. Wang, H.; Tian, Q.; Shen, Y.; Yu, T. Non-isolated three-port converter with wide operating range and low EMI characteristics. *Sci. Technol. Vis.* **2021**, *3*, 34–39. [[CrossRef](#)]
13. Pourjafar, S.; Shayeghi, H.; Sedaghati, F.; Seyedshenava, S.; Blaabjerg, F. A bidirectional multiport DC-DC converter applied for energy storage system with hybrid energy sources. *Int. J. Circ. Theor. Appl.* **2021**, *49*, 2453–2478. [[CrossRef](#)]

14. Shayeghi, H.; Pourjafar, S.; Hashemzadeh, S.M. A Switching Capacitor based Multi-Port Bidirectional DC-DC Converter. *IET Power Electron.* **2021**, *14*, 1622–1636. [[CrossRef](#)]
15. Yi, W.; Ma, H.; Peng, S.; Liu, D.; Ali, Z.M.; Dampage, U.; Hajjiah, A. Analysis and implementation of multi-port bidirectional converter for hybrid energy systems. *Energy Rep.* **2022**, *8*, 1538–1549. [[CrossRef](#)]
16. Suresh, K.; Bharatiraja, C.; Chellammal, N.; Tariq, M.; Chakraborty, R.K.; Ryan, M.J.; Alamri, B. A Multifunctional Non-Isolated Dual Input-Dual Output Converter for Electric Vehicle Applications. *IEEE Access* **2021**, *9*, 64445–64460. [[CrossRef](#)]
17. Zhang, J.; Wu, H.; Huang, J.; Xing, Y.; Ma, X. Research on Multi-port Bidirectional Buck-Boost Converter. *Power Electron.* **2021**, *55*, 129–135. [[CrossRef](#)]
18. Jiang, L.; Fan, J.; Zhang, W.; He, D.; Liao, Z. Simulation Study of Three-Port DC/DC Converters. *China Comput. Commun.* **2021**, *33*, 1–4.
19. Shao, Z. Analysis of a non-transformer isolated three-port converter with single input and dual output operation mode. *J. Xuchang Univ.* **2019**, *38*, 131–133.
20. Moradisizkoochi, H.; Elsayad, N.; Mohammed, O.A. An Integrated Interleaved Ultrahigh Step-Up DC–DC Converter Using Dual Cross-Coupled Inductors With Built-In Input Current Balancing for Electric Vehicles. *IEEE J. Emerg. Sel. Top. Power Electron.* **2019**, *8*, 644–657. [[CrossRef](#)]
21. Kumar, A.; Sensarma, P. Ripple-Free Input Current High Voltage Gain DC-DC Converters With Coupled Inductors. *IEEE Trans. Power Electron.* **2019**, *34*, 3418–3428. [[CrossRef](#)]
22. Faraji, R.; Farzanehfard, H. Soft-Switched Nonisolated High Step-Up Three-Port DC–DC Converter for Hybrid Energy Systems. *IEEE Trans. Power Electron.* **2018**, *33*, 10101–10111. [[CrossRef](#)]
23. Kardan, F.; Alizadeh, R.; Banaei, M.R. A novel step-up multi-input DC-DC converter for hybrid electric vehicles application. *IEEE Trans. Power Electron.* **2017**, *32*, 3549–3561. [[CrossRef](#)]
24. Kardan, F.; Alizadeh, R.; Banaei, M. A New Three Input DC/DC Converter for Hybrid PV/FC/Battery Applications. *IEEE J. Emerg. Sel. Top. Power Electron.* **2017**, *5*, 1771–1778. [[CrossRef](#)]
25. Jalilzadeh, T.; Rostami, N.; Babaei, E.; Hosseini, S.H. Bidirectional Multi-Port DC-DC Converter with Low Voltage Stress on Switches and Diodes. *IET Power Electron.* **2020**, *13*, 1593–1604. [[CrossRef](#)]
26. Liu, J.; Hu, R.; Zeng, J. Non-isolated three-port converter with high gain. *Trans. China Electrotech. Soc.* **2019**, *34*, 10. [[CrossRef](#)]
27. Ma, S.; Pan, T. Switched-Capacitor Based Three-Port DC-DC Converters. *J. Power Supply* **2015**, *13*, 48–55. [[CrossRef](#)]
28. Wang, H.; Chen, Y.; Zeng, Q.; Li, S.; Zhu, B. A Multi-Condition High Gain Multi-Port DC/DC Converter. *Proc. CSEE* **2019**, *39*, 2155–2166. [[CrossRef](#)]
29. Fares, A.M.; Klumpner, C.; Sumner, M. A Novel Multiport DC-DC Converter for Enhancing the Design and Performance of Battery—Supercapacitor Hybrid Energy Storage Systems for Unmanned Aerial Vehicles. *Appl. Sci.* **2022**, *12*, 2767. [[CrossRef](#)]
30. Santosh Kumar Reddy, P.; Obulesu, Y. Design and Development of a New Transformerless Multi-port DC-DC Boost Converter. *J. Electr. Eng. Technol.* **2022**, *14*, 23–38. [[CrossRef](#)]
31. Suntiom, T.; Messo, T.; Puukko, J. *Power Electronic Converters—Dynamics and Control in Conventional and Renewable Energy Applications*; John Wiley & Sons: Weinheim, Germany, 2017. [[CrossRef](#)]
32. Venkataramana, S. Small Signal Modeling of Non-Isolated High Gain DC-DC converter. In Proceedings of the 2020 International Conference for Emerging Technology (INCET), Belgaum, India, 5–7 June 2020. [[CrossRef](#)]

Disclaimer/Publisher’s Note: The statements, opinions and data contained in all publications are solely those of the individual author(s) and contributor(s) and not of MDPI and/or the editor(s). MDPI and/or the editor(s) disclaim responsibility for any injury to people or property resulting from any ideas, methods, instructions or products referred to in the content.